Medical Image Analysis 99 (2025) 103328

Contents lists available at ScienceDirect

Medical Image Analysis

journal homepage: www.elsevier.com/locate/media

Learning lifespan brain anatomical correspondence via cortical developmental continuity transfer

Lu Zhang [a], Zhengwang Wu [b], Xiaowei Yu [a], Yanjun Lyu [a], Zihao Wu [c], Haixing Dai [c], Lin Zhao [c], Li Wang [b], Gang Li [b], Xianqiao Wang [d], Tianming Liu [c], Dajiang Zhu [a,*]

[a] Department of Computer Science and Engineering, The University of Texas at Arlington, Arlington, TX, 76019, USA
[b] Department of Radiology and BRIC, University of North Carolina at Chapel Hill, Chapel Hill, NC, 27599, USA
[c] Department of Computer Science, University of Georgia, Athens, GA, 30602, USA
[d] College of Engineering, University of Georgia, Athens, GA, 30602, USA

ARTICLE INFO

Keywords:
Transfer learning
Common and group-specific patterns
Lifespan correspondence
Developmental continuity

ABSTRACT

Identifying anatomical correspondences in the human brain throughout the lifespan is an essential prerequisite for studying brain development and aging. But given the tremendous individual variability in cortical folding patterns, the heterogeneity of different neurodevelopmental stages, and the scarce of neuroimaging data, it is difficult to infer reliable lifespan anatomical correspondence at finer scales. To solve this problem, in this work, we take the advantage of the developmental continuity of the cerebral cortex and propose a novel transfer learning strategy: the model is trained from scratch using the age group with the largest sample size, and then is transferred and adapted to the other groups following the cortical developmental trajectory. A novel loss function is designed to ensure that during the transfer process the common patterns will be extracted and preserved, while the group-specific new patterns will be captured. The proposed framework was evaluated using multiple datasets covering four lifespan age groups with 1,000+ brains (from 34 gestational weeks to young adult). Our experimental results show that: 1) the proposed transfer strategy can dramatically improve the model performance on populations (e.g., early neurodevelopment) with very limited number of training samples; and 2) with the transfer learning we are able to robustly infer the complicated many-to-many anatomical correspondences among different brains at different neurodevelopmental stages. (Code will be released soon: https://github.com/qidianzl/CDC-transfer).

1. Introduction

The mammalian cerebral cortex is characterized by complex folding, which folds during the early brain development. Normal cortical growth and folding patterns are crucial for the brain circuitry and its functional organization (Shipp (2007)). Many brain function malformations, cognitive deficits, and mental disorders have shown close relationship to abnormalities in cortical folding caused by abnormal or interrupted neuronal development (Stutterd & Leventer (2014); Fern´andez et al. (2016); Di Donato et al. (2017)). Therefore, understanding the development of the cortical folding pattern has long been an important topic. However, the cortical folding pattern varies strikingly across individuals and shows tremendous heterogeneity across different neurodevelopmental stages. Building reliable lifespan anatomical correspondences, which aims to align cortex across individuals from different neurodevelopmental stages to establish longitudinal cross-subject correspondences, is an essential task and prerequisite for longitudinal studies of revealing brain developmental trajectories over age or estimating the brain anatomy-function relationship (Honey et al. (2010); Derrfuss & Mar (2009); Giedd & Rapoport (2010)).

To this end, brain atlases are commonly employed for cross-subject alignment, wherein the same atlas is aligned to different individual brains. However, this approach heavily relies on the regularity and commonality of anatomical structures, potentially ignoring individual differences. To address this limitation, researchers have explored finer gyral-sulcal cortical landscapes that enhance correspondence in brain alignment. One notable advancement involves the utilization of sulcal fundi as effective landmarks to improve the accuracy of cortex alignment (Pantazis et al. (2010); Desai et al. (2005); Van Essen (2005)). Additionally, another study unveiled the presence of indivisible units

---

* Corresponding author.
E-mail address: dajiang.zhu@uta.edu (D. Zhu).

https://doi.org/10.1016/j.media.2024.103328
Received 6 December 2023; Received in revised form 4 July 2024; Accepted 26 August 2024
Available online 30 August 2024

known as sulcal roots, which demonstrated a consistent organizational pattern across individuals during the fetal stage. These studies have demonstrated that meaningful cortical landmarks at finer resolutions can effectively decompose relatively large cortical folds into more specific, atomic, and depictive units, thereby improving brain alignment accuracy. A recent breakthrough in the field has led to the identification of a new landmark that characterizes the cortical folding pattern at a finer resolution. This novel landmark, known as the 3-hinge gyrus (3HG), is defined as the convergence of gyri from three directions (Fig. 1 (B)). Extensive studies have confirmed that 3HGs are evolutionarily preserved across multiple primate species (Li et al. (2017)), robustly existed on human brains despite different populations or brain conditions (Chen et al. (2017); Ge et al. (2018); Zhang et al. (2020d, c)) and possessing both common and individual patterns (Zhang et al. (2023)).

Since 3HGs are identified in the individual space, to find reliable corresponding 3HGs across different brains, several methods (Zhang et al. (2020c, 2023)) have been proposed. However, these methods are designed to find the 3HG correspondences in single cohort, typically the adult cohort. When applied to lifespan study including multiple neurodevelopmental stages, existing approaches typically either mix all stages and only train a single model or learn an independent model from scratch for each stage. The former strategy ignores the heterogeneity of different neurodevelopmental stages and can only obtain the common pattern shared by all states. Consequently, our understanding of the dynamic nature of neurodevelopmental processes remains limited. On the other hand, the second strategy fails to leverage the intrinsic relationships that exist across neurodevelopmental stages. This approach not only requires large datasets for each stage but also lacks the efficiency of utilizing shared knowledge and learned representations across different stages. Unfortunately, acquiring data for early neurodevelopmental stages can be particularly challenging due to factors such as high acquisition costs, prevalent motion artifacts, and subject dropout rates. Consequently, the populations at many early neurodevelopmental stages in lifespan brain imaging dataset often have very limited samples and is insufficient to train an independent model from scratch. It thus would be beneficial if we can take the advantage of the intrinsic relationship between different stages to facilitate the transfer of shared patterns across different neurodevelopmental stages.

In deep learning domain, Transfer Learning (TL) (Pan & Yang (2009); Woodworth & Thorndike (1901)) has emerged as a powerful technique for leveraging shared features across related domains. It allows us to harness the knowledge gained from a source domain and apply it to improve learning performance or reduce the reliance on labeled examples in a target domain. It is of particular significance when tackling tasks with limited samples and has shown superior performances in image classification (Long et al. (2015)), segmentation (Van Opbroek et al. (2014)), text sentiment classification (Blitzer et al. (2006)), and disease prediction (Khan et al. (2019)), etc. Inspired by these successful studies, in this work, we aim to design a novel transfer strategy to leverage the inherent relationship between different age groups to facilitate the transfer of shared patterns across neurodevelopmental stages.

As the cortical folding undergoing and neurodevelopment progressing, the anatomical patterns of two close neurodevelopmental stages share more commonalities, especially during the adult stage. To take advantage of this type of cortical developmental continuity, we proposed a novel cortical developmental continuity (CDC) transfer framework (Fig. 1 (A)). Specifically, we trained the model from scratch by the age group with the largest sample size and then transferred and adapted the well-trained model to the other stages following the cortical developmental trajectory. A novel loss function is designed to ensure that during the transfer process the common patterns will be extracted and

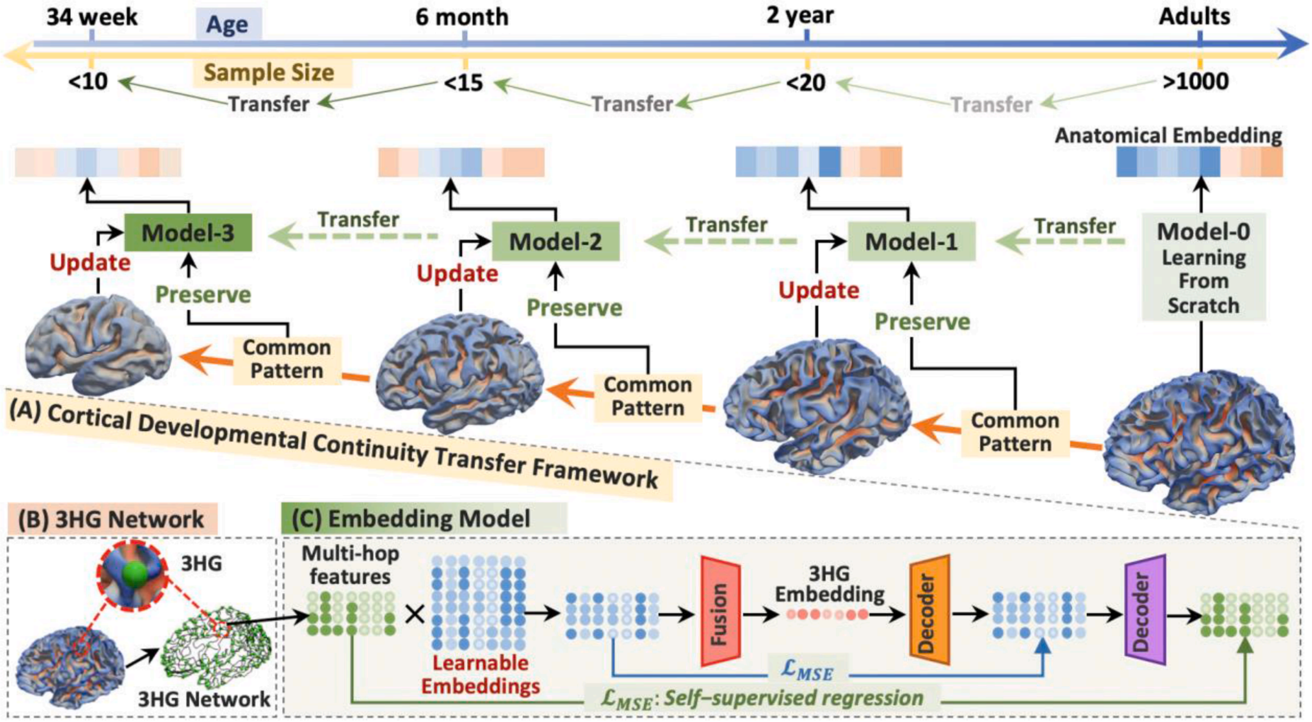

Fig. 1. (A) The overall scheme of the proposed framework. The embedding model is trained from scratch by the adult group which has the most data samples and then successively transferred and adapted to other age groups, following the developmental trajectory of the cerebral cortex (Section 3.2). The detailed architecture of the embedding model is displayed in (C). (B) We used the 3HG network to describe the brain anatomy. Each 3HG is the conjunction of gyri from three directions and the 3HGs on the same hemisphere are connected by gyri hinges into a network (Section 3.1). For each 3HG, we used the anatomical regions it located in and its multi-hop connections with other 3HGs as two key features to generate multi-hop features, which is used as a data sample in the learning process (Section 3.1). (C) the embedding model adopted two-level encoding architecture to hierarchically map the input multi-hop features in a latent representation for each 3HG (Section 3.1).

preserved, while the stage-specific new patterns will be captured. We applied our method on four age groups using adult HCP dataset and pediatric datasets with 1,000+ brains (from 34 gestational weeks to young adult). Our experimental results show that: 1) the proposed transfer strategy can dramatically improve the model performance on populations (e.g., early neurodevelopment) with very limited training samples; and 2) with the transfer learning we are able to robustly infer the complicated many-to-many anatomical correspondences among different brains at the same and/or different neurodevelopmental stages.

2. Related works

2.1. Methods for inferring 3HG correspondences

Establishing 3HG cross-subject correspondence is a significant yet under-researched topic. Two existing studies have attempted to address this issue from different perspectives. In 2020, Zhang et al. (2020c) proposed a two-view, group-wise graph matching method leveraging both cortical folding patterns and DTI-derived fiber shapes to estimate 3HG correspondences. Their approach aims to jointly optimize anatomical topological patterns and axonal connectivity as two views, maximizing the consistency between corresponding 3HGs across different brains. However, this method faces three challenges: Firstly, the robustness and computational time depend heavily on the number of samples due to the group-wise optimization scheme. Secondly, the method performs independent graph matching from scratch, limiting its ability to generalize 3HG correspondences to new brains and new datasets. Thirdly, the features of the two views are handcrafted, which weakens the method's adaptability to individual variations, potentially undermining its effectiveness.

To address these limitations, Zhang et al. (2023) developed a learning-based embedding framework that can effectively encode individual cortical folding patterns into a group of anatomically meaningful feature embeddings. Within this framework, each 3HG is represented by a combination of these feature embeddings, utilizing individual-specific combining coefficients. This approach enables the encoding of regular folding patterns within the embedding vectors while preserving individual variations through the combination coefficients. This method has successfully been applied to infer anatomical correspondences among adult cohorts. However, a limitation of this self-supervised embedding approach is its reliance on large datasets during the training step. This poses a challenge when applying this method to brain longitudinal studies, as populations in some early neurodevelopmental stages often consist of a limited number of samples. Training a reliable embedding model from scratch becomes unfeasible in such scenarios. To solve this problem, we take the advantage of the developmental continuity of the cerebral cortex and proposed a novel CDC transfer framework. This framework leverages the inherent relationship between different age groups to facilitate the transfer of shared patterns across neurodevelopmental stages.

2.2. Transfer learning in medical image analysis

Over the past decade, deep learning (DL) techniques (Wang et al. (2021); Zhou et al. (2023)) have significantly advanced various domains of computer vision, particularly in tasks such as classification (Abdar et al. (2021); Díaz-Pernas et al. (2021)) and segmentation (Khan et al. (2020)) for medical image analysis. Unlike traditional machine learning approaches that rely on shallow architectures, DL architectures eliminate the need for manual feature engineering (LeCun et al. (2015)). This absence of feature engineering is advantageous because it removes the constraints imposed by feature selection, thereby maximizing the information available for classification tasks. However, the effectiveness of DL models hinges on the availability of large annotated datasets for training. Acquiring such datasets, especially in the medical domain, poses substantial challenges due to high costs associated with image collection. Furthermore, the complexity increases when these datasets need to be annotated by professional radiologists, whose expertise ensures accurate labeling but also adds significant additional expenses. In some cases, the costs incurred from annotation can exceed those of image acquisition itself. To mitigate these difficulties, researchers have introduced transfer learning (Pan & Yang (2009); Woodworth & Thorndike (1901)) techniques into the field of medical image analysis. Unlike traditional machine learning algorithms that focus on isolated tasks, transfer learning leverages knowledge learned from source tasks to enhance learning in related target tasks. This advantage stems from transfer learning models being pre-trained on extensive generic datasets, with task-specific datasets used solely for fine-tuning the model.

Over the past decades, transfer learning has been extensively applied across various imaging anatomy domains, covering the brain (Deepak et al. (2020); Mehrotra et al. (2020); Plata et al. (2017)), heart (Liao et al. (2020)), chest (Khan et al. (2021); Polat et al. (2021)), abdomen (Meng et al. (2020); Peng et al. (2019)), breast (Yap et al. (2017)), skin (Liu et al. (2020)), and retinal (Hervella et al. (2020)) areas. These studies span multiple imaging modalities including Computed Tomography (CT) (Khan et al. (2021); Liao et al. (2020)), Magnetic Resonance Imaging (MRI) (Deepak et al. (2020); Mehrotra et al. (2020); Plata et al. (2017); Liao et al. (2020)), Ultrasound (US) (Yap et al. (2017); Meng et al. (2020)), and Radiography (X-rays) (Polat et al. (2021)). CNN-based architectures such as LeNet (Yap et al. (2017)), U-Net (Hervella et al. (2020); Liao et al. (2020)), AlexNet (Deepak et al. (2020); Mehrotra et al. (2020); Plata et al. (2017)), VGGNet (Deepak et al. (2020); Meng et al. (2020)), ResNet (Deepak et al. (2020); Mehrotra et al. (2020); Liao et al. (2020)), GoogLeNet (Deepak et al. (2020); Mehrotra et al. (2020)), DenseNet (Khan et al. (2021); Polat et al. (2021)), and SqueezeNet (Mehrotra et al. (2020)) are the most widely used transfer learning models for medical image analysis. These networks were initially trained on the ImageNet dataset and subsequently adapted to medical image datasets. However, while transferring pre-trained models trained on natural image datasets like ImageNet has proven successful in many applications, challenges arise due to differences in characteristics between medical images and natural images, leading to suboptimal results in some medical imaging tasks.

Inspired by the knowledge transfer capabilities of transfer learning and aiming to mitigate ineffective results stemming from disparities between the source and target domains, we introduced a CDC transfer framework for inferring lifespan brain anatomical correspondence. The CDC transfer strategy capitalizes on the developmental continuity of the brain, enabling the capture and transfer of common patterns across various developmental stages. This approach efficiently utilizes limited samples to capture group-specific patterns, enhancing training efficiency. Importantly, all transfer learning operations are conducted within the same domain, ensuring effective knowledge transfer without the inefficiencies associated with cross-domain adaptation.

3. Methods

The CDC framework is grounded in the fundamental principle of continuous brain development, aiming to leverage the inherent relationship between different age groups to facilitate the transfer of shared patterns across neurodevelopmental stages. This is accomplished by a sequential learning process that initiates with the age group possessing the largest sample size for robustness and generalizability. Then, the learned knowledge is transferred to other age groups, following the developmental trajectory of the cerebral cortex. This approach facilitates the propagation of common patterns throughout the learning process, while effectively utilizing the limited samples to capture group-specific patterns.

To ensure that this manuscript is self-contained, we firstly introduced the 3HG identification (Chen et al. (2017)) and 3HG embedding (Zhang et al. (2023)) in Section 3.1, offering the necessary background information. Following that, in Section 3.2, we have elaborated on the proposed CDC transfer framework

3.1. Background

3.1.1. 3HG identification

The process of 3HG identification consists of five steps, as depicted in Fig. 2. Firstly, the entire cerebral cortex is segmented into gyral crest and sulcal basins based on the gyral altitude (Fig. 2(a and b)). Subsequently, a tree marching algorithm is employed to connect all the vertices of the gyral crest, resulting in a graph representation (Fig. 2(c)). In the next step, redundant branches shorter than a predefined threshold are trimmed, while the main trunks are preserved (Fig. 2(d and e)). The resulting graph is referred to as GyralNet. 3HGs are defined as the conjunctions with three branches on the Gyralnet. Finally, the entire cortex of each hemisphere is divided into 75 regions of interest (ROIs) by surface parcellation with the Destrieux Atlas (Destrieux et al. (2010)). Each 3HG belongs to one specific ROI (Fig. (2f)), and this association is numerically represented using one-hot encoding with a 1D vector of size 75: $x \in R^{1\ \times\ 75}$.

3.1.2. 3HG anatomical embedding

Based on the insights from Zhang et al. (2023), the 3HG anatomical embedding is highlighted as a more effective representation of 3HG anatomical patterns compared to one-hot encoding. This forms the basis of the proposed CDC transfer framework. In this subsection, we provide a brief overview of the 3HG anatomical embedding.

The 3HG network (GyralNet) can be represented by a graph $\mathscr{G} = (\mathscr{A}, \mathscr{X})$, where the adjacency matrix $\mathscr{A} = [a_{i,j}] \in R^{N\times N}$ represents the direct connections between N 3HGs (nodes) and the one-hot encoding matrix (feature matrix) $\mathscr{X} = \{x_1; x_2; \cdots; x_N\} \in R^{N\times\ 75}$ represents the association between N 3HGs and 75 ROIs. To capture indirect connections between nodes at different hop levels, the l^{th} power of $\mathscr{A}$, denoted as $\mathscr{A}^l$, is used to represent the $l^{th} - hop$ indirect connections. Consequently, the l^{th} $-hop$ feature of $3HG_i$ can be obtained by multiplying $\mathbf{a}_i^l$, the i^{th} row of $\mathscr{A}^l$, with $\mathscr{X}$. Using these definitions, we can formulate the $l -hop$ feature of $3HG_i$ as (1). This $l - hop$ feature encompasses the features from the 0^{th} $-hop$ to the $l^{th} - hop$, capturing the connection patterns of $3HG_i$ with other nodes in the network at various hop distances.

$$F_l^i = \left[x_i;\ \mathbf{a}_i^1\mathscr{X};\ \mathbf{a}_i^2\mathscr{X};\ \cdots; \mathbf{a}_i^l\mathscr{X}\right] \in R^{(l+1)\ \times\ 75} \tag{1}$$

Taking F_l^i as input, a self-supervised embedding framework (Fig. 1 (C)) is designed to learn meaningful feature embedding for each ROI, just like the word embedding in NLP. The encoding and decoding processes can be formulated as:

$$E_H^i = \sigma\left(F_l^i \cdot \mathbb{E}\right) \tag{2}$$

$$E_F^i = \sigma\left(W^F \cdot E_H^i\right) \tag{3}$$

$$\widehat{E}_H^i = \sigma\left(W^{D_1} \cdot E_F^i\right) \tag{4}$$

$$\widehat{F}_l^i = \widehat{E}_H^i \cdot W^{D_2} \tag{5}$$

where σ is the non-linear activation function and $\mathbb{E} = \{AptCommandmathbbe_1; AptCommandmathbbe_2; \cdots; AptCommandmathbbe_{75}\} \in R^{75\ \times d}$ is the learnable ROI embeddings. The input feature (F_l^i) was firstly embedded via $\mathbb{E}$ hop by hop to generate the hierarchical multi-hop embeddings $E_H^i \in R^{(l+1)\ \times\ \mathrm{d}}$, and then was further fused into a single embedding vector $E_F^i \in R^{1\ \times\ \mathrm{d}}$ by $W^F \in R^{1\ \times\ (l+1)}$. The MSE loss is adopted to evaluate the two-level decoding ($W^{D_1} \in R^{(l+1)\ \times\ 1}$ and $W^{D_2} \in R^{d\times\ 75}$) and the objective function is defined as (6):

$$\mathscr{L} = \alpha \parallel E_H^i - \widehat{E}_H^i\|_F^2 + \beta\| F_l^i - \widehat{F}_l^i \|_F^2 \tag{6}$$

In our proposed CDC transfer framework, the same embedding architecture was employed as the initial model to learn the ROI embeddings $\mathbb{E}$ from scratch, using data samples of adult group. Subsequently, we proposed a novel CDC transfer strategy to transfer and adapt $\mathbb{E}$ to other age groups, following the developmental trajectory of the cerebral cortex. This transfer process allowed us to leverage the accumulated knowledge and apply it to characterize both the common and the group-specific anatomical patterns across different age groups.

3.2. Cortical Developmental Continuity (CDC) transfer framework

CDC transfer framework is proposed to take the advantage of the continuous nature of the development of cortical folding and achieve the optimal performance improvement (Fig. 1 (A)). Specifically, we adopt shared ROIs across all neurodevelopmental stages as features and define a common feature space. This allows data samples from different age groups to be mapped to the same feature space and to be represented in a consistent multi-hop form (Section 3.1). Taking the 3HG multi-hop features as input, the embedding framework (Section 3.1) is trained from scratch by the age group with the largest data samples to endow the model with good generalizability. Then the learned ROI feature embeddings $\mathbb{E}$ is transferred and adapted to the next age group. During the transfer process, the common pattern buried in $\mathbb{E}$ is gradually extracted and combined with the new group-specific patterns learned from new data samples. Finally, the combination of the common patterns and the group specific patterns is used to create the ROI embeddings for that group and then transferred to another age group in the following steps. To maximize the effectiveness, the transfer process follows the cortical developmental trajectory from one age group to the next closest age group, since they tend to share the greatest consistency.

Fig. 3 illustrates the transfer process between four age groups within the CDC framework. The embedding framework is initially trained from scratch by group 1, utilizing a self-supervised task to learn the ROI feature embeddings $\mathbb{E}_1$ specific to group 1. Subsequently, $\mathbb{E}_1$ is transferred to group 2, which is the closest age group to group 1. During the transfer process, $\mathbb{E}_1$ can be divided into two components: the common pattern shared by groups 1 and 2, and the specific pattern unique to group 1. The goal is to transfer the common pattern to group 2, allowing data samples from group 2 to be effectively utilized for learning the

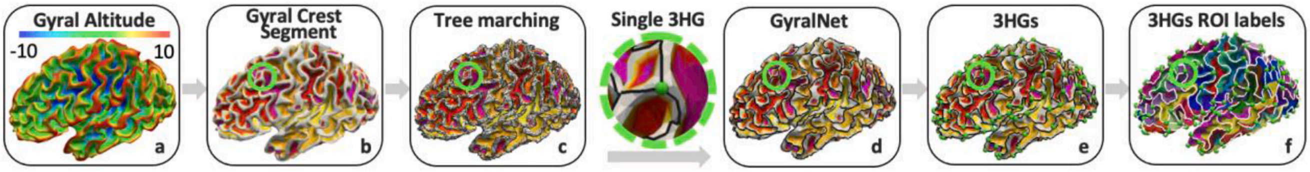

Fig. 2. Pipeline of 3HGs identification. a: White matter surface is reconstructed, and color coded by gyri altitude. b: The watershed algorithm is applied on the gyral altitude map to divide the surface into gyral crest (white regions) and sulcal basins (colorful regions). c: A tree marching algorithm is used to connect vertices in gyral crest regions. d-e: Redundant branches are trimmed when their length is shorter than a predefined threshold, and the main trunk remained is the 3HG network, which is termed GyralNet in (Zhang et al. (2020c)). f: Each 3HG is labeled by the region of interest (ROI) it belongs to.

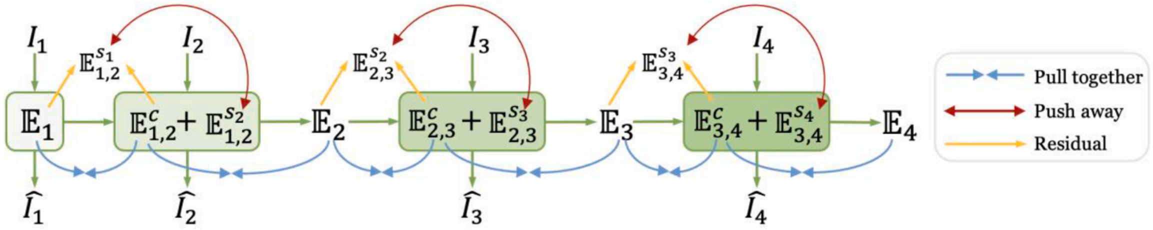

Fig. 3. Illustration of the transfer process in the proposed cortical developmental continuity (CDC) transfer framework. The diagram demonstrates the transfer process within the framework using four groups as an example. Each group (labeled as group 1, group 2, group 3, and group 4) possesses its own set of input samples (I_i) and obtained the corresponding output ($\widehat{I_i}$). Each age group learns its own fusion layer and two decoder layers ($W^{F},\ W^{D_1}$, and W^{D_2}), while the learning process of embedding $\mathbb{E}_i$ is guided by CDC transfer strategy. Specifically, the embedding framework is trained from scratch using group 1′s input samples, resulting in the generation of the ROI feature embedding ($\mathbb{E}_1$). During the training process, a common part, denoted as $\mathbb{E}^c_{1,2}$, is extracted from $\mathbb{E}_1$, representing the shared features between group 1 and group 2. This common part is combined with the group-specific embeddings ($\mathbb{E}^{s_2}_{1,2}$) learned by group 2, resulting in the ROI feature embedding for group 2. This process is repeated by each pair of adjacent groups, including groups 1 and 2, groups 2 and 3, and so on, transferring the learned ROI embeddings successively from one group to the closest neighboring group.

specific patterns of group 2. To achieve this, a new group-specific embedding matrix $\mathbb{E}^{s_2}_{1,2}$ is initialized to capture the group-specific patterns of group 2. Simultaneously, the common pattern $\mathbb{E}^c_{1,2}$ is initialized with $\mathbb{E}_1$ and iteratively updated during the training process. Consequently, the ROI feature embeddings of group 2, denoted as $\mathbb{E}_2$, are obtained as the sum of $\mathbb{E}^c_{1,2}$ and $\mathbb{E}^{s_2}_{1,2}$: $\mathbb{E}_2 = \mathbb{E}^c_{1,2} + \mathbb{E}^{s_2}_{1,2}$. The residual part between the original $\mathbb{E}_1$ and the updated $\mathbb{E}^c_{1,2}$ represents the specific pattern of group 1. To ensure that the learned $\mathbb{E}^c_{1,2}$ indeed captures the common pattern shared by the two groups, and that $\mathbb{E}^{s_2}_{1,2}$ accurately captures the group-specific pattern of group 2, two regularizers are proposed and defined as follows:

$$\mathscr{L}_{spe} = \max\left(0, \cos\left(\mathbb{E}^{s_1}_{1,2},\ \mathbb{E}^{s_2}_{1,2}\right) - m\right),\ m \in (-1,\ 1) \tag{7}$$

$$\mathscr{L}_{com} = 2 - \cos\left(\mathbb{E}^c_{1,2},\ \mathbb{E}_1\right) - \cos\left(\mathbb{E}^c_{1,2},\ \mathbb{E}_2\right) \tag{8}$$

The two regularizers proposed in the CDC framework utilize cosine similarity, which is a common measure to assess the similarity or dissimilarity between two inputs in nonlinear embedding learning or semi-supervised learning scenarios. The first regularizer, $\mathscr{L}_{spe}$, aims to push away the two group-specific embeddings, $\mathbb{E}^{s_1}_{1,2}$ and $\mathbb{E}^{s_2}_{1,2}$, by ensuring a minimum distance between them. The hyperparameter m defines the lower bound distance to be maintained. The second regularizer, $\mathscr{L}_{com}$, works to bring the common part, $\mathbb{E}^c_{1,2}$, closer to both ROI embeddings $\mathbb{E}_1$ and $\mathbb{E}_2$. This regularizer encourages the shared patterns to align with both groups, enhancing the transfer of common knowledge. In (7) and (8), we illustrate the application of the two regularizers using groups 1 and 2 as examples. These regularizers are consistently applied during the transfer process for each pair of adjacent groups, including groups 1 and 2, groups 2 and 3, and so on. Their purpose is to preserve the distinction between group-specific patterns while promoting alignment of common patterns across groups. The whole transfer learning process is guided by the reconstruction objective function (6) and constrained by the two regularizers.

3.3. Evaluation methods

The proposed framework is evaluated from three perspectives:

3.3.1. Effectiveness of ROI embedding

The ROI embeddings are obtained by recovering the multi-hop connection patterns of 3HGs at a population level, serving as fundamental components for representing each 3HG. Consequently, the ROI embeddings are expected to effectively capture the regularity of the anatomical pattern among 3HGs within the population. The strength of the 3HG's $l-hop$ connection is adopted to describe the anatomical pattern of 3HGs, which refers to the number of edges with a length of l that connect two ROIs in the 3HG network. If two ROIs have a high/low $l-hop$ strength, it indicates that they are strongly/weakly connected in the 3HG network at the $l-hop$ level. As a result, their $l-hop$ embeddings should exhibit a corresponding high/low similarity in the embedding space.

3.3.2. Effectiveness of inferring lifespan 3HG correspondences

The primary motivation of this work is to establish reliable brain anatomical longitudinal correspondences. To evaluate this, we applied the generated 3HG embeddings to the task of inferring complicated many-to-many cross-subject and cross-group anatomical correspondences of 3HGs. An effective 3HG embedding vector is expected to preserve the individuality of 3HGs while providing reliable cross-subject and cross-group 3HG anatomical correspondences.

3.3.3. Comparison of different transfer strategies

Ablation studies were conducted to evaluate each component of the proposed CDC transfer framework and compare the performance of different transfer strategies and brain atlases with different granularity.

4. Results

We conducted experiments with four age groups: adult (22-35Y), 2-year (2Y), 6-month (6M), and 34-gestational-week (34W, preterm). For each group, we applied the proposed multi-hop feature embedding method (Section 3.1) to the identified 3HGs (Section 3.1). Initially, we trained the model from scratch using the adult group, which provided the largest data sample. Subsequently, we sequentially transferred the well-trained model to the other three age groups: 2-year, 6-month, and finally the 34-week group. For each age group, the model was trained end-to-end in a self-supervised manner. To evaluate the effectiveness of the learned ROI feature embeddings ($\mathbb{E}$) for each age group, we analyzed the strength of the 3HG's $l-hop$ connection (Section 3.3). Furthermore, we extended the learned ROI embeddings and the well-trained model to the independent testing dataset, generating individual embedding vectors for each 3HG. The efficacy of these generated 3HG embeddings was assessed in the task of lifespan anatomical correspondence, enabling inference of cross-subject and cross-group anatomical correspondences.

The Result Section is organized as follows: Section 4.1 introduces the experimental setting; Section 4.2 evaluates the effectiveness of the learned ROI embeddings; Section 4.3 presents the results of lifespan 3HG correspondences; and Section 4.4 is the ablation study which compares the influence of different regularizers, different transfer strategies, and brain atlases with different granularity.

4.1. Experimental setting

4.1.1. Data setting

In this work, we used structural MRI of 1,064 adults from Human Connectome Project (HCP) S1200 release. The detailed imaging parameters can be referred to (Zhang et al. (2020b, 2022)). We followed the standardized pre-processing procedures outlined in (Zhang et al. (2021, 2020a)) for imaging data. These steps included brain skull removal, tissue segmentation, and cortical surface reconstruction by FreeSurfer package (Fischl (2012)). To demonstrate the effectiveness of proposed CDC transfer strategy, we only used pediatric structural MRI of 30/30/10 subjects in 2-year/6-month/34-week groups from NDA and dHCP datasets. All pediatric images were processed with an infant-dedicated pipeline (http://www.ibeat.cloud/) (Wang et al. (2023)). Destrieux parcellation (Destrieux et al. (2010)) was used to conduct ROI labeling for all the four age groups. After pre-processing, 400/164/500 training/validation/testing splitting was adopted for the adult group, 10/10/10 training/validation/testing splitting was adopted for 2Y and 6M groups, and 5/2/3 training/validation/testing splitting was adopted for the 34W group.

4.1.2. Model setting

For multi-hop features, we compared 1-hop ($l = 1$ in (1)), 2-hop, and 3-hop feature embedding for adult group and transferred the model of 1-hop and 2-hop embedding to other age groups since they provide better results. In our experiments, when training from scratch with the adult group, the ROI embeddings $\mathbb{E}$ was initialized by identity matrix with dimension $d = 128$ to ensure equal initial distance between any two ROI embeddings. The other layers, including fusion layer (W^F) and two decoder layers (W^{D_1} and W^{D_2}), were implemented by fully connected layers and initialized following the Xavier scheme. The hyper-parameters α and β were both set to 1.0. We employed the non-linear activation function σ as *relu*. The Adam optimizer was used to train the whole model with standard learning rate 0.001, weight decay 0.01, and momentum rates (0.9, 0.999). The embedding framework comprises a learnable embedding layer $\mathbb{E} = \quad \in R^{75\times d}$, a fusion layer $W^F \in R^{1\times(l+1)}$, and two decoder layers $W^{D_1} \in R^{(l+1)\times 1}$ and $W^{D_2} \in R^{d\times 75}$. The total number of parameters is $150\,d + 2(l+1) \approx 20k$. Consequently, the parameter count is small, resulting in very fast training. Training from scratch with approximately 400K 3HGs from 1000 adult subjects takes about 4 hours using a GTX 1080 Ti GPU.

4.2. Evaluation of ROI embeddings

We conducted an evaluation of the learned ROI embeddings by using the strength of 3HG's $l-hop$ connection, as described in Section 3.1. The results are presented in Fig. 4. Fig. 4(a) presents the results of ROI embeddings learned by training from scratch with the adult group. The first column of Fig. 4(a) displays the connection strength, which serves as the ground truth, is calculated using the entire population of 1,064 subjects from the adult group to ensure statistical representativeness. The second column of Fig. 4(a) displays the cosine similarity between the learned ROI embedding vectors. To facilitate analysis, we divided the 3HG's multi-hop connections into three types: gyri-gyri connections (top left of each matrix), gyri-sulci connections (top right and bottom left), and sulci-sulci connections (bottom right). These connections refer to the relationships between gyral regions, between gyral and sulcal regions, and between sulcal regions, respectively. The results for different hops are displayed in separate rows.

Since 3-hop connections (the third row) cover a larger range of the cerebral cortex and connect remote regions that cannot be directly connected by 1-hop and 2-hop connections, ROI pairs with weak 1-hop and 2-hop connections may exhibit strong 3-hop connections. This can lead to inaccurate representation of the connection strength between ROI pairs. As a result, the learned embedding vectors of these regions

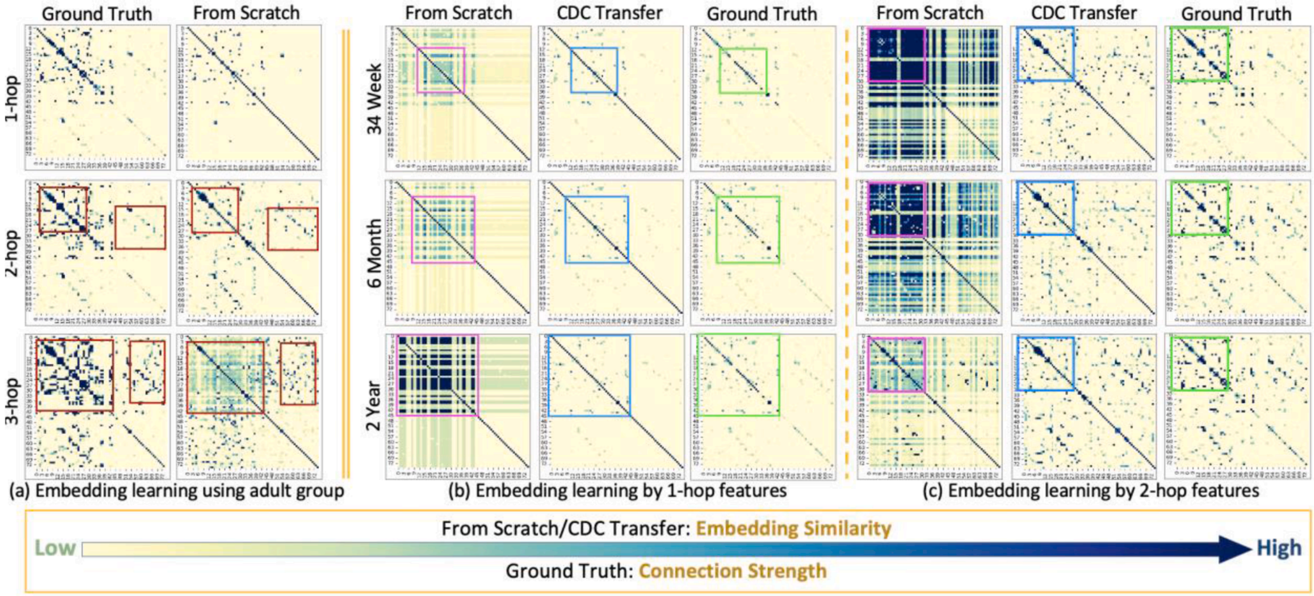

Fig. 4. Evaluation of the learned ROI embeddings using strength of the 3HG's $l-hop$ connection (defined in Section 3.1). (a) The first column displays the strength of the 3HG's 1-hop, 2-hop, and 3-hop connections, which were calculated based on the whole population of the adult group consisting of 1,064 subjects. The results of the three different hops are presented in three separate rows. The second column shows the embedding similarity matrices, which were obtained by calculating the cosine similarity between pairs of ROI embeddings. These ROI embeddings were learned from scratch using the training dataset of the adult group. (b) The well-trained model for 1-hop embedding, as obtained in (a), was sequentially transferred by CDC transfer strategy to the 2-year group, then to the 6-month group, and finally to the 34-week group. The embedding similarity matrices of the learned ROI embeddings are presented in the second column. Additionally, for each group, a model was trained from scratch using the same training dataset, and the embedding similarity matrices of the learned ROI embeddings are shown in the first column. The third column displays the connection strength matrices (ground truth), which were calculated based on the whole population of each age group. (c) Similar to (b), this subfigure presents the results of the 2-hop embedding. The order of the brain regions in all the matrices in (a), (b), and (c) corresponds to the order defined in the Destrieux atlas (Destrieux et al. (2010)), where the first 44 regions primarily represent gyri, while the remaining 31 regions represent sulci.

show approximate similarities and form a smooth square at the top-left corner (the third row of Fig. 4(a)), which undermines the effectiveness of the ROI embeddings. In contrast, 1-hop and 2-hop embeddings provide better results. Therefore, we only transferred the well-trained models of 1-hop and 2-hop embeddings to the other three age groups and displayed the results of CDC transfer framework in the second column of Fig. 4(b) and (c), respectively. In addition, to illustrate the superiority of the CDC transfer framework, for each age group, we trained a model from scratch using the same training dataset and displayed the results in the first column of Fig. 4(b) and (c). The connection strength (ground truth) is shown in the third column.

It is important to note that the ground truth matrix represents the strength of actual anatomical connections between ROIs in the cortical space, whereas the embedding similarity matrix depicts the cosine similarity between the learned ROI embedding vectors, representing the relationship between ROIs in the embedding space. Hence, the presence of similar patterns in the two matrices indicates that the learned ROI embeddings effectively capture the common anatomical patterns.

We can see that for both 1-hop (Fig. 4(b)) and 2-hop (Fig. 4(c)) embeddings, when trained from scratch, most gyri-gyri connections (top left of each matrix) areas of the similarity matrices in the ROI embeddings appear as patches with the same color (highlighted by pink squares). This indicates that the regions covered by each patch share the same similarity. However, in the corresponding locations of the ground truth matrices, the connection strength between these regions exhibits noticeable differences (highlighted by green squares). In contrast, the embedding similarity matrices obtained through the CDC transfer framework successfully capture these differences and display patterns that are highly similar to the ground truth matrices. These results indicate that the ROI embeddings learned by the CDC transfer framework accurately capture the common patterns. More specifically, when two ROIs have strong or weak connections in cortical space (3HG network), they also exhibit correspondingly high or low similarities in the embedding space.

In addition to visualization, we conducted quantitative analysis using three measures: cosine similarity (CS), structural similarity index measure (SSIM), and Pearson correlation coefficient (PCC), to assess the similarity between the ground truth and the learned embeddings. The results for 1-hop and 2-hop embedding were reported in Tables 1 and 2, respectively. In these tables, the measures are calculated between the embedding similarity matrices obtained from different methods (rows) and the ground truth matrices of different age groups (columns). The values calculated between two matrices from the same age group are highlighted with colorful borders.

We analyzed the results from two perspectives. Firstly, for each age group, larger values of the three measures between the learned embedding matrices and the corresponding ground truth matrices (within the colorful blocks) indicate the superiority of the respective method. From the tables we can see that for both 1-hop and 2-hop embeddings, the three measures obtained from the CDC transfer strategy (the second row in colorful blocks) show significant improvements compared to training from scratch (the first row in colorful blocks). Secondly, we evaluated whether the learned embeddings could capture group-specific patterns while avoiding trapping into common patterns of the overall population. To assess this, we highlighted the highest values of the three measures with a blue color. To capture the group-specific pattern, the highest values should be obtained between the learned embedding similarity matrix and the ground truth matrix from the same age group (within the colorful blocks). Therefore, the presence of more highest values marked with blue color within the colorful blocks indicates the superior performance of the corresponding method. From the tables we can see that for the CDC transfer framework, nearly all the largest values are located within the colorful blocks. In contrast, when training from scratch, most of the largest values are obtained outside the colorful blocks. These results suggest that the proposed CDC transfer strategy can effectively improve the embedding effectiveness and capture the group-specific patterns.

4.3. *3HGs longitudinal correspondences*

For each age group, we applied the learned ROI embeddings and the well-trained model to the testing dataset to generate 3HG embeddings – E_F^i (defined in (3)). As discussed in Section 3.1, an effective 3HG embedding is expected to be able to provide reliable longitudinal cross-subject 3HG correspondences as well as preserve the individuality.

4.3.1. *Inferring reliable lifespan 3HG correspondences*

We randomly selected a subject (sub-0 in Figs. 5 and 6) and employed its 3HGs as the exemplars to infer the corresponding 3HGs in other subjects across different age groups. For each exemplar 3HG, the inference process involved the following steps: 1) for each 3HG in different subjects from different age groups, the cosine similarity between its embedding vector with the embedding vector of the exemplar 3HG was calculated; 2) for each subject, the corresponding 3HGs were identified by selecting the ones that had a cosine similarity of 1.0 to the exemplar 3HG; 3) If no 3HGs had a cosine similarity of 1.0 to the exemplar 3HG, the 3HG with the highest cosine similarity (above a predefined threshold) was chosen as the corresponding 3HG. By following these steps, the corresponding 3HGs for each exemplar 3HG in different subjects were obtained.

To provide a clearer visualization, we selected 35 exemplar 3HGs from sub-0 that spanned the entire cerebral cortex. In Fig. 5 (1-hop embedding) and Fig. 6 (2-hop embedding), we showed the corresponding 3HGs of these exemplars in 15 randomly selected subjects (sub-1 to sub-15) from 4 age groups, obtained using different methods. The locations of the 3HGs are represented by bubbles, and the corresponding 3HGs in different subjects are denoted by the same color. To evaluate the accuracy of the different methods in inferring lifespan 3HG

Table 1
1-Hop embedding similarity.

Emb. \ GT		34W			6M			2Y			Adult		
		CS	SSIM	PCC	CS	SSIM	PCC	CS	SSIM	PCC	CS	SSIM	PCC
34W	FS	0.445	0.227	0.438	0.445	0.231	0.436	0.449	0.232	0.439	0.416	0.219	0.410
	CDC	0.613	0.771	0.605	0.597	0.777	0.589	0.601	0.770	0.593	0.556	0.768	0.548
6M	FS	0.478	0.294	0.473	0.480	0.295	0.473	0.487	0.296	0.480	0.446	0.288	0.442
	CDC	0.593	0.759	0.585	0.610	0.764	0.602	0.598	0.758	0.590	0.553	0.757	0.545
2Y	FS	0.409	0.266	0.400	0.409	0.269	0.392	0.412	0.270	0.395	0.382	0.260	0.369
	CDC	0.586	0.724	0.579	0.593	0.724	0.584	0.604	0.729	0.596	0.546	0.722	0.539

Emb.: Embeddings; **GT:** Ground Truth; **FS:** Training From Scratch; **CDC:** CDC Transfer; Blue values: the largest values of each measure for each group; Colorful bounder: the embeddings and the ground truth are from the same group.

Table 2
2-Hop embedding similarity.

Emb. \ GT		34W			6M			2Y			Adult		
		CS	SSIM	PCC	CS	SSIM	PCC	CS	SSIM	PCC	CS	SSIM	PCC
34W	FS	0.423	0.125	0.398	0.424	0.130	0.392	0.428	0.131	0.398	0.399	0.116	0.377
	CDC	0.597	0.572	0.581	0.574	0.568	0.558	0.584	0.571	0.567	0.526	0.546	0.510
6M	FS	0.415	0.081	0.390	0.420	0.083	0.389	0.425	0.084	0.400	0.389	0.074	0.366
	CDC	0.556	0.452	0.538	0.600	0.463	0.582	0.591	0.462	0.573	0.513	0.435	0.495
2Y	FS	0.462	0.206	0.438	0.471	0.210	0.443	0.481	0.211	0.456	0.433	0.194	0.410
	CDC	0.554	0.501	0.536	0.578	0.512	0.560	0.596	0.513	0.579	0.511	0.486	0.493

Emb.: Embeddings; **GT:** Ground Truth; **FS:** Training From Scratch; **CDC:** CDC Transfer; Blue values: the largest values of each measure for each group; Colorful bounder: the embeddings and the ground truth are from the same group.

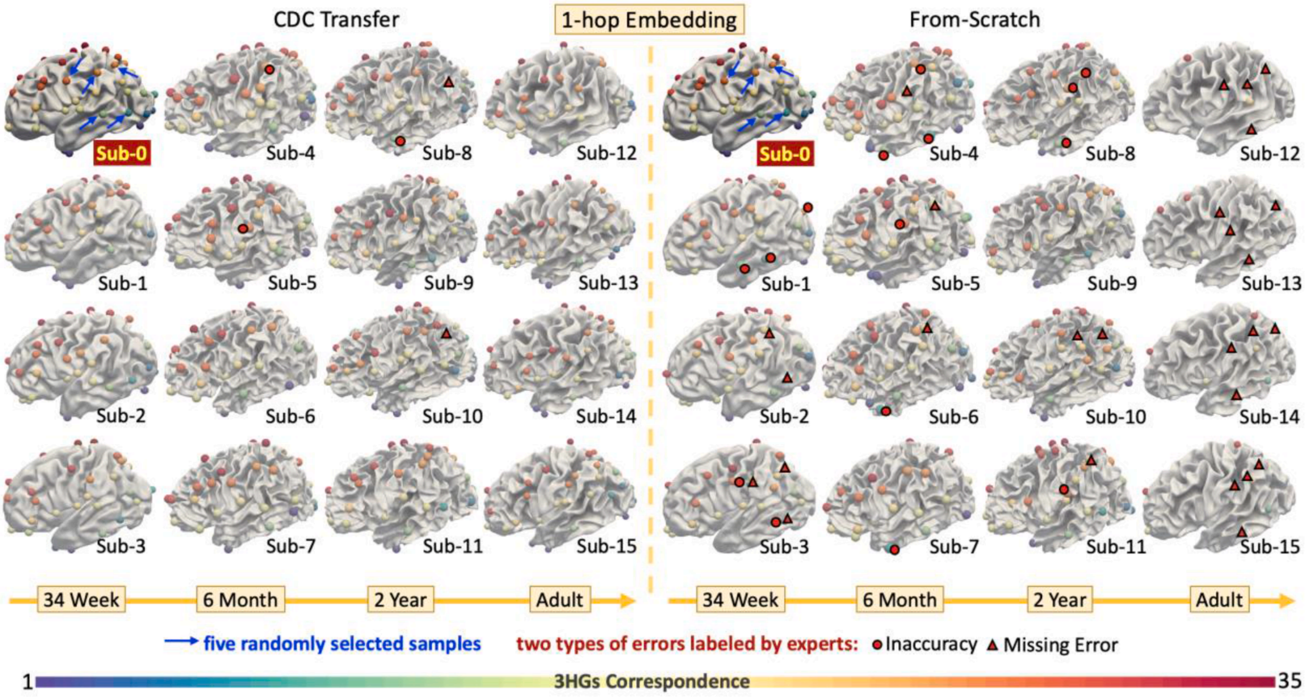

Fig. 5. Lifespan correspondences of 3HGs via 1-hop embedding. The 3HGs of a randomly selected subject in 34W group (sub-0) were used as exemplary 3HGs. To find the corresponding 3HGs on other subjects, the following pipeline was adopted: 1) for each 3HG in different subjects from different age groups, the cosine similarity between its embedding vector with the embedding vector of the exemplar 3HG was calculated; 2) for each subject, the corresponding 3HGs were identified by selecting the 3HGs that had a cosine similarity of 1.0 to the exemplar 3HG; 3) If no 3HGs had a cosine similarity of 1.0 to the exemplar 3HG, the 3HG with the highest cosine similarity (above a predefined threshold) was chosen as the corresponding 3HG. Following these steps, the corresponding 3HGs for each exemplar 3HG in different subjects were obtained. For better visualization, we selected 35 exemplar 3HGs from sub-0 that spanned the entire cerebral cortex and showed the corresponding 3HGs in 15 randomly selected subjects (from sub-1 to sub-15) from 4 age groups, obtained using different methods. The corresponding 3HGs in different subjects are represented using the same color. Two experts were involved to evaluate the correspondence results and two kinds of errors: inaccuracy/missing error, are marked by red circle/triangle with black border.

correspondences, we involved two experts who identified and labeled two types of correspondence errors: 1) inaccuracy error, which means that the identified corresponding 3HGs are not the best matches. Inaccuracy errors were marked by red circles with black border; and 2) missing error, which means the corresponding 3HGs were not identified. The missing errors were marked by red triangles with black, pointing to the location of the correct corresponding 3HG.

The results demonstrate that the corresponding 3HGs identified using the CDC transfer strategy consistently align with the common anatomical landscapes across individuals of different age groups. There were two inaccuracy errors (sub4, sub8) and two missing errors (sub8, sub10) in the 1-hop embedding results, and one inaccuracy error (sub-3) and one missing error (sub-5) in the 2-hop embedding results. Comparatively, when trained from scratch, there were significantly more errors, with 14 inaccuracy errors and 27 missing errors in the 1-hop embedding, and 14 inaccuracy errors and 26 missing errors in the 2-hop embedding. Furthermore, there were no noticeable differences in the quality of correspondences between the age groups using the CDC transfer strategy. However, when trained from scratch, there were substantial differences in correspondence performance among the age groups. For instance, the results for the adult group were notably worse, with nearly all corresponding 3HGs missing. These findings indicate that the proposed CDC framework provides an effective approach for designing practical pre-training paradigms and facilitating downstream tasks in brain longitudinal studies.

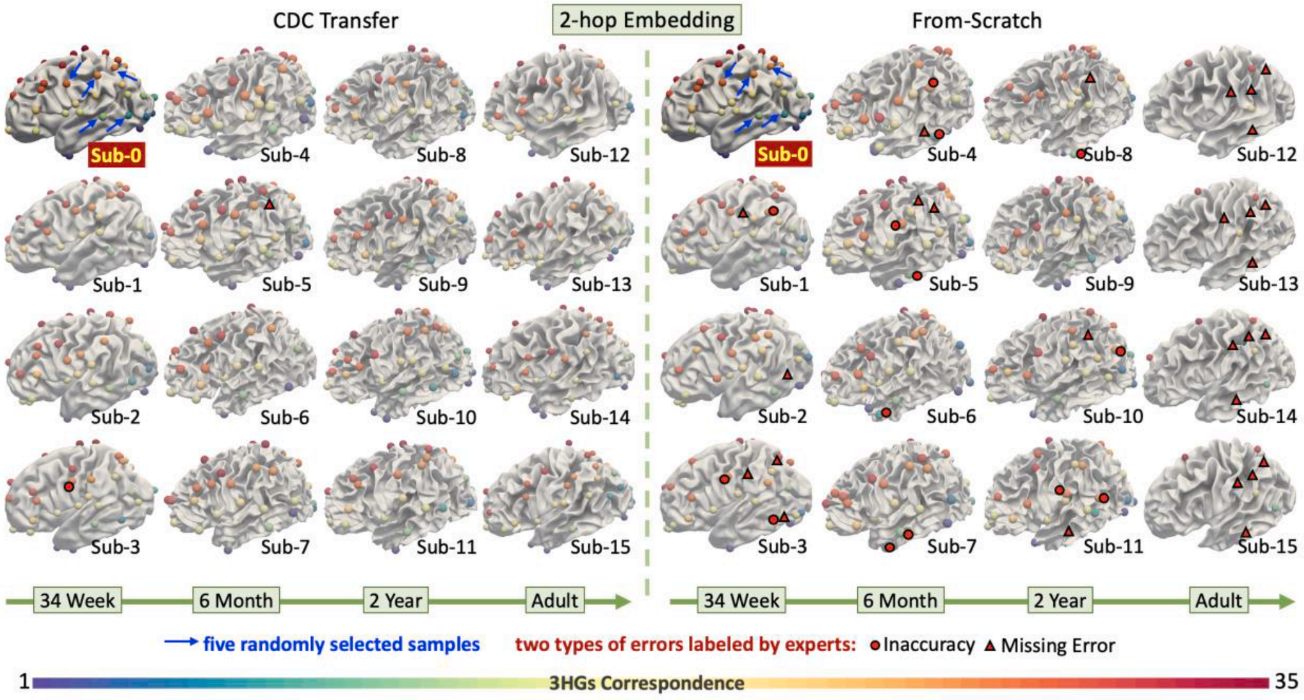

Fig. 6. Lifespan correspondences of 3HGs via 2-hop embedding. The detailed description can be referred to Fig. 5.

4.3.2. *Preserving the individuality*

Cross-subject intensive variability is a crucial characteristic exhibited by the human cerebral cortex. To demonstrate the capability of the learned 3HG embeddings to capture cross-subject individuality, we randomly selected four 3HGs located at different positions on the cerebral cortex as exemplars (pointed by yellow arrows) and identified their corresponding 3HGs in different subjects. For each subject, any 3HGs with a cosine similarity greater than 0.9 to the exemplar 3HG were identified as corresponding 3HGs. We randomly chose three subjects from each of the four age groups (34W, 6M, 2Y, and adult) and presented the results in Fig. 7. Distinct folding patterns are observed in the cerebral cortex of the 12 subjects. For instance, consider the exemplar 3HG-1 situated at the conjunction of the middle frontal gyrus and precentral gyrus, where no other 3HGs are found nearby. However, for the first subject in adult group (marked by green arrow), the cortical folding patterns exhibit greater complexity. As a result, multiple 3HGs are clustered together at that specific location. Conversely, for the second subject in adult group (marked by pink arrow), there is no convergence between the middle frontal gyrus and the precentral gyrus, leading to the absence of 3HGs in that area. More examples have been marked in the remaining three exemplars. These results indicate that the 3HG embeddings learned by CDC transfer framework can effectively preserve the individual variabilities.

4.4. *Ablation study*

4.4.1. *Comparison of different regularizers*

In CDC transfer, two regularizers $\mathscr{L}_{spe}$ and $\mathscr{L}_{com}$ are used to guide the model in capturing common and group-specific patterns. To assess the impact of these regularizers on the embedding performance, we conducted an ablation study. Specifically, we compared the embedding performance across four settings for each age group: with only $\mathscr{L}_{com}$, with only $\mathscr{L}_{spe}$, without both $\mathscr{L}_{spe}$ and $\mathscr{L}_{com}$, and the CDC transfer with both $\mathscr{L}_{spe}$ and $\mathscr{L}_{com}$. The results are reported in Table 3.

We analyzed the results from two perspectives. Firstly, we focused on the values of the three measures within the colorful blocks, where the embedding matrix and the corresponding ground truth matrix belong to the same group. A higher value of the three measures indicates greater similarity between the two matrices, thus demonstrating the effectiveness of the corresponding method. As shown in Table 3, within each colorful block, the three measures obtained from the other three settings displayed a significant decrease compared to CDC transfer. For example, in the 2Y group (pink block), the SSIM measure between the embedding matrix learned via CDC transfer and the ground truth matrix was 0.513, whereas it dropped to 0.403 and 0.269 with a single regularizer. When trained without any regularizers, it further decreased to 0.184. Secondly, for each method (row), we highlighted the highest values of the three measures with a blue color. Similar with the analysis of Table 1 and 2, the presence of more highest values marked with blue color within the colorful blocks indicates the superior performance of the corresponding method in capturing group-specific pattern. From the results we can see that for the CDC transfer framework, all the largest values are located within the colorful blocks. In contrast, many of the largest values under the other three settings are obtained outside the colorful blocks. These findings suggest that both regularizers are necessary for accurately capturing group-specific patterns.

In addition to the embedding performance, we also evaluated the training efficiency by examining the convergence curves obtained using the independent validation dataset, as shown in Fig. 8. We can see that for all the three age groups, 34W (Fig. 8 (a)), 6M (Fig. 8 (b)), and 2Y (Fig. 8 (c)), when compared to training from scratch, the four transfer settings can achieve remarkably better results with significantly lower loss. Moreover, among the four transfer settings, the proposed CDC transfer with both regularizers demonstrates faster convergence towards a better solution.

4.4.2. *Comparison with other transfer strategies*

In the proposed CDC transfer, we adopted a specific type of transfer strategy where the embedding transfer traverses all previous age groups before reaching the target group. For example, in the case of the 34W group, the embedding transfer starts from the adult group and sequentially transfers to the 2Y, 6M, and finally to the 34W group. To explore the necessity of traversing all previous groups, we conducted experiments and compared different transfer strategies, the results of which

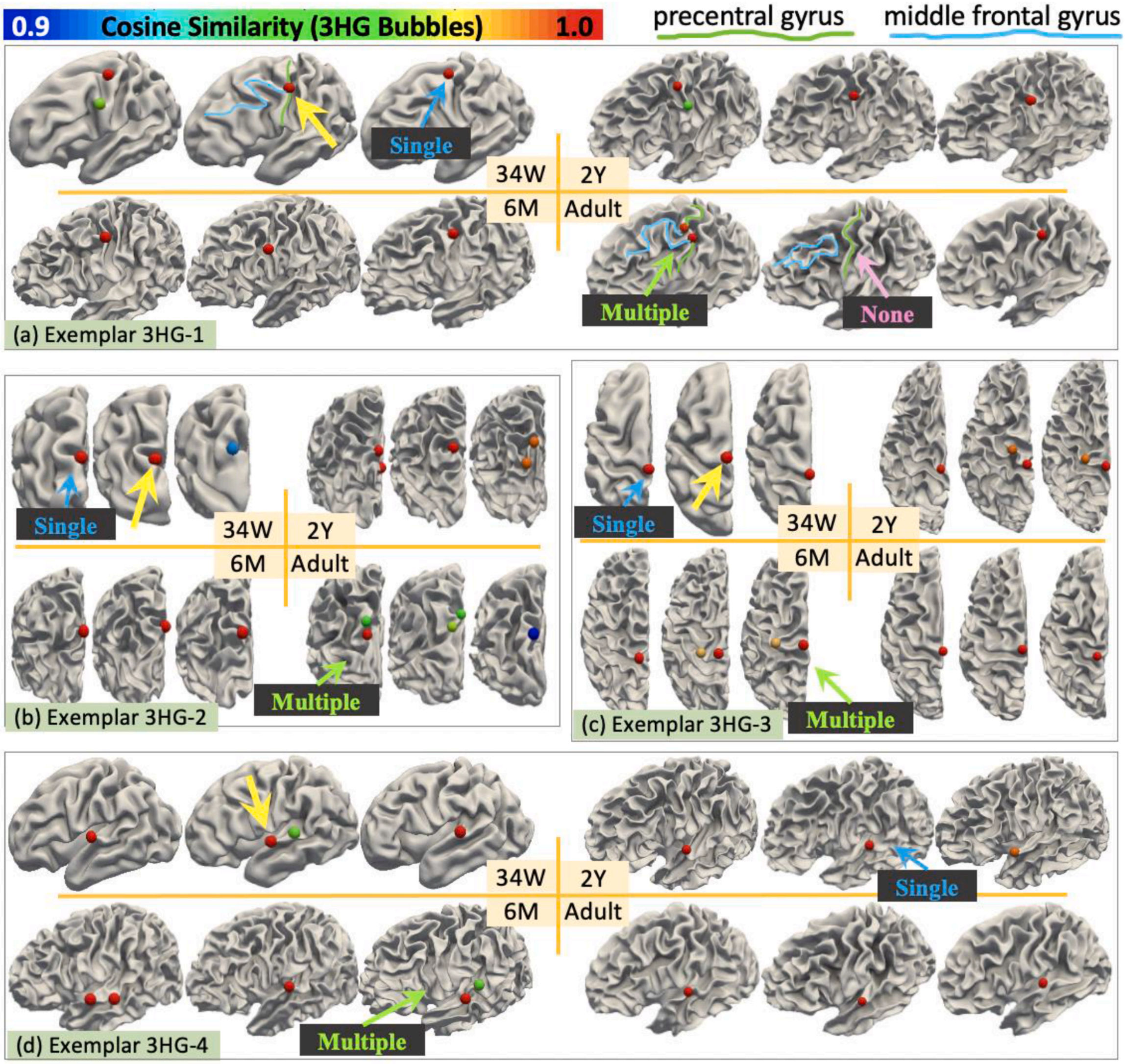

Fig. 7. Cross-subject individuality and variability. We selected four exemplar 3HGs (indicated by yellow arrows) to examine their correspondences in subjects from four different age groups (34W, 6M, 2Y, and Adult). For each age group, we randomly selected three subjects and established correspondences based on a cosine similarity threshold of 0.9. The corresponding 3HGs are visualized as bubbles, with the color of the bubbles indicating the cosine similarity. Given the intensive variability of cerebral cortex, it is possible to find varying numbers of correspondences, ranging from zero to multiple, across different subjects.

are presented in Table 4. For 34W and 6M groups, there are three and two different transfer strategies, respectively.

From the results, two key observations can be made. Firstly, different transfer strategies achieve comparable performance with approximate values of the three measures between the embedding matrices and the ground truth matrices from the same age group (within colorful blocks); Secondly, the transfer strategy that involves traversing all previous groups tends to outperform others in capturing group-specific patterns. For example, in the case of the 6M group, when the model was directly transferred from the adult group, skipping the 2Y group, the highest value of SSIM was obtained between the embedding matrix of the 6M group and the ground truth matrix of the 2Y group (highlighted in blue). However, when the model traversed all the groups, the highest values of the three measures were obtained between the embedding matrix and the ground truth matrix of the 6M group, indicating a better capture of group-specific patterns. Additionally, the convergence curves of the five transfer strategies are presented in Fig. 8 (d). It can be observed that models trained using more groups exhibit faster convergence.

4.4.3. Comparison of different brain atlases

The ROI embeddings serve as the features of 3HGs and play an important role in the embedding learning and 3HG correspondence. In this section, we discussed the influence of the brain atlases with different levels of granularity on the performance. Specifically, we used three different atlases: the Desikan-Killiany Atlas (Desikan et al., 2006) with 72 ROIs, the Destrieux Atlas (Destrieux et al., 2010) with 150 ROIs, and the gwMRF parcellations with 1000 ROIs (Schaefer et al., 2018). For the Desikan-Killiany and Destrieux atlases, we used the Freesurfer package (Fischl (2012)) to map the atlases to the individual brain, and for the gwMRF 1000 atlas, we used the code and method released by the authors (https://github.com/ThomasYeoLab/CBIG/tree/master/stable_projects/brain_parcellation/Schaefer2018_LocalGlobal) to map the atlas to the individual brain. We displayed the three different atlases in Fig. 9a. We also calculated the average number of 3HGs per ROI and the mean cosine similarity between corresponding 3HGs of the three atlases. The mean cosine similarity is calculated as follows: for each anchor 3HG, we identified the top-1 corresponding 3HG with the greatest cosine similarity value in each subject. Then we calculated the mean cosine similarity across all the anchor 3HGs and population. From the results, we can see that as the granularity increases, the area covered by each ROI generally decreases, and thus the mean 3HG number decreases. For the mean cosine similarity, compared to the other two atlases, the

Table 3
Evaluation of the two regularizers.

GT / Emb.		34W			6M			2Y			Adult		
		CS	SSIM	PCC	CS	SSIM	PCC	CS	SSIM	PCC	CS	SSIM	PCC
34W	$\mathcal{L}_{com}$	0.489	0.293	0.472	0.495	0.290	0.477	0.510	0.291	0.493	0.431	0.277	0.413
	$\mathcal{L}_{spe}$	0.543	0.458	0.528	0.546	0.454	0.531	0.560	0.455	0.546	0.484	0.436	0.469
	No	0.465	0.248	0.450	0.470	0.243	0.454	0.486	0.244	0.472	0.403	0.234	0.388
	CDC	0.597	0.572	0.581	0.574	0.568	0.558	0.584	0.571	0.567	0.526	0.546	0.510
6M	$\mathcal{L}_{com}$	0.466	0.236	0.446	0.511	0.244	0.491	0.516	0.243	0.496	0.417	0.226	0.397
	$\mathcal{L}_{spe}$	0.488	0.298	0.469	0.539	0.310	0.521	0.544	0.307	0.526	0.438	0.285	0.419
	No	0.432	0.252	0.412	0.489	0.263	0.469	0.495	0.260	0.476	0.382	0.242	0.361
	CDC	0.556	0.452	0.538	0.600	0.463	0.582	0.591	0.462	0.573	0.513	0.435	0.495
2Y	$\mathcal{L}_{com}$	0.464	0.259	0.445	0.496	0.267	0.478	0.517	0.269	0.500	0.419	0.251	0.401
	$\mathcal{L}_{spe}$	0.487	0.385	0.471	0.517	0.399	0.502	0.539	0.403	0.525	0.443	0.376	0.427
	No	0.419	0.180	0.396	0.448	0.183	0.425	0.469	0.184	0.448	0.372	0.171	0.350
	CDC	0.554	0.501	0.536	0.578	0.512	0.560	0.596	0.513	0.579	0.511	0.486	0.493

Emb.: Embeddings; **GT:** Ground Truth; **CDC:** CDC Transfer; Blue values: the largest values of each measure for each training strategy; Colorful bounder: the embeddings and the ground truth are from the same group.

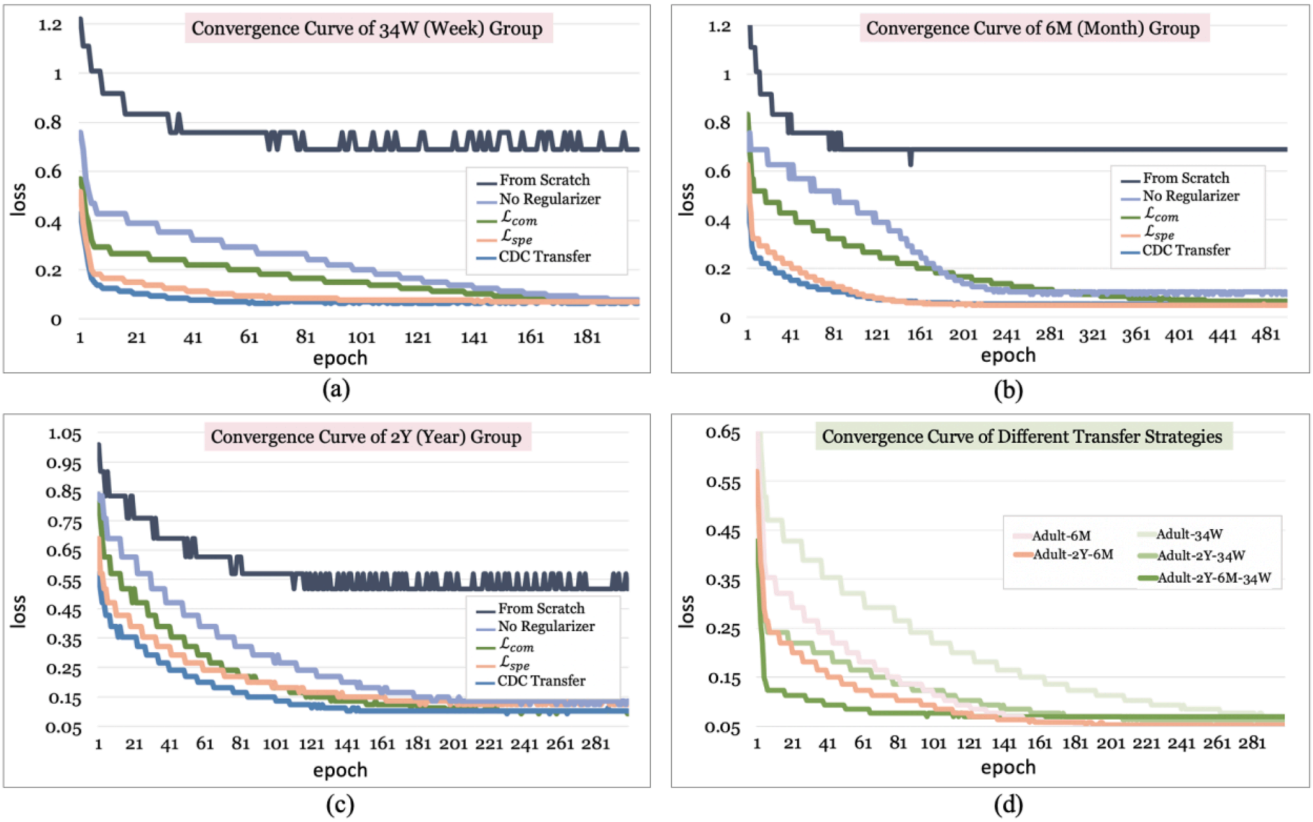

(a) (b) (c) (d)

Fig. 8. Convergence curves of different regularizer settings (a-c) and different transfer strategies (d).

gwMRF 1000 has significantly lower values. This indicates that the embedding vectors between corresponding 3HGs have lower similarity. To better analyze this difference, we showed the embedding matrices learned using different atlases in Fig. 9c and d.

From Fig. 9c, we can see that as the granularity increases, the sparsity of the ground truth matrices also increases. Similarly, the patterns of the embedding matrices are consistent with the ground truth matrices. To quantitatively measure this, we calculated the sparsity of the ground truth matrices for each atlas, as shown in Fig. 9d. Consistent with the visualization results, the sparsity values increase as the granularity increases. We also used three different measures to check the similarity between the learned embedding matrices and the ground truth matrices, and all three atlases show high similarity between the two matrices. Of all the four measures, only the change in sparsity trends correlates with the change in mean cosine similarity. We infer that as granularity increases, the brain is divided into more regions, leading to more regions

Table 4
Comparison of different transfer strategies.

GT / Emb.		34W			6M			2Y			Adult		
		CS	SSIM	PCC	CS	SSIM	PCC	CS	SSIM	PCC	CS	SSIM	PCC
34W	Adult-34W	0.592	0.555	0.576	0.567	0.552	0.551	0.578	0.553	0.561	0.520	0.531	0.503
	Adult-2Y-34W	0.591	0.552	0.575	0.567	0.549	0.551	0.576	0.551	0.560	0.519	0.528	0.503
	Adult-2Y-6M-34W	0.597	0.572	0.581	0.574	0.568	0.558	0.584	0.571	0.567	0.526	0.546	0.510
6M	Adult-6M	0.557	0.452	0.539	0.600	0.463	0.580	0.591	0.464	0.573	0.514	0.435	0.496
	Adult-2Y-6M	0.556	0.452	0.538	0.600	0.463	0.582	0.591	0.462	0.573	0.513	0.435	0.495

Emb.: Embeddings; **GT:** Ground Truth; Blue values: the largest values of each measure for each training strategy; Colorful bounder: the embeddings and the ground truth are from the same group.

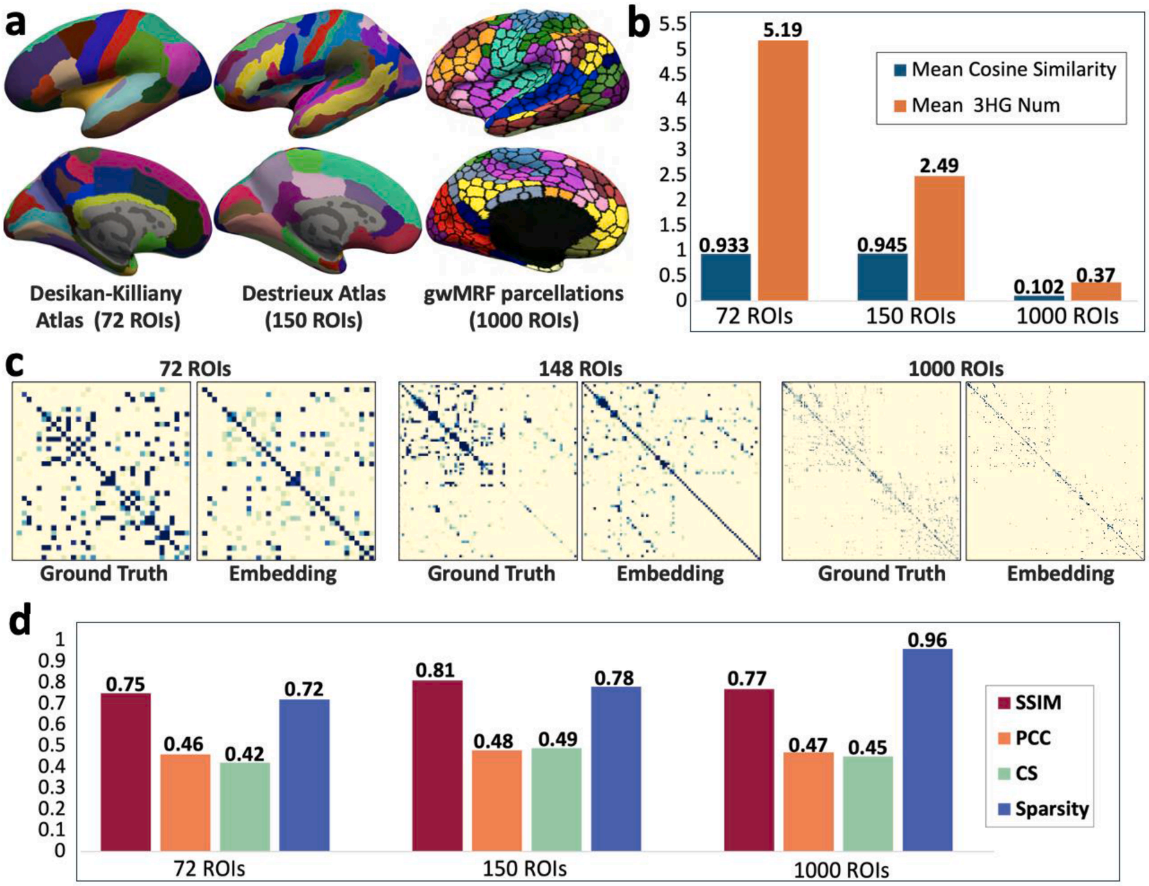

Fig. 9. Comparison of different atlases. **a**. The three different atlases at different levels of granularity. **b**. The mean cosine similarity of top-1 corresponding 3HGs and the average number of 3HGs per ROI of the three atlases. **c**. The learned embedding similarity matrices and the corresponding ground truth matrices of three different atlases. **d**. Four measures are used to test the similarity between the ground truth and the learned embedding matrices as well as the sparsity of these matrices.

without 3HGs and thus increasing sparsity. Because many regions lack 3HGs to mediate connections with other regions, the overall correlation between regions decreases. This results in a lower cosine similarity between the learned embedding vectors.

To further investigate the impact of atlas granularity on the 3HG correspondence task, we selected four anchor 3HGs (highlighted by yellow arrows) from various brain regions and inferred their corresponding 3HGs in other subjects. Based on the statistical results shown in Fig. 9b, we set a cosine similarity threshold of 0.9 for the Desikan-Killiany and Destrieux atlases to identify corresponding 3HGs. Specifically, any 3HG with a cosine similarity value of 0.9 or higher is considered a corresponding 3HG to the anchor 3HG. For the gwMRF1000 atlas, we used a threshold of 0.05 for identifying corresponding 3HGs. We showed the results of six randomly selected subjects in Fig. 10. In the figure, the identified corresponding 3HGs in each subject are represented by bubbles, and the cosine similarity is color-coded. For each subject, there are three cerebral cortex sections corresponding to three subfigures, arranged from left to right in increasing granularity: 72 ROIs, 150 ROIs, and 1000 ROIs. As the granularity increases, we can see that the number of identified corresponding 3HGs in each subject decreases, which is consistent with the mean 3HG number values shown in Fig. 9b. Additionally, the distribution of the corresponding 3HGs gradually becomes more localized around the region of the anchor 3HG, resulting in more precise identification. However, when the granularity becomes too high, such as at 1000 regions, some existing corresponding 3HGs may be missed

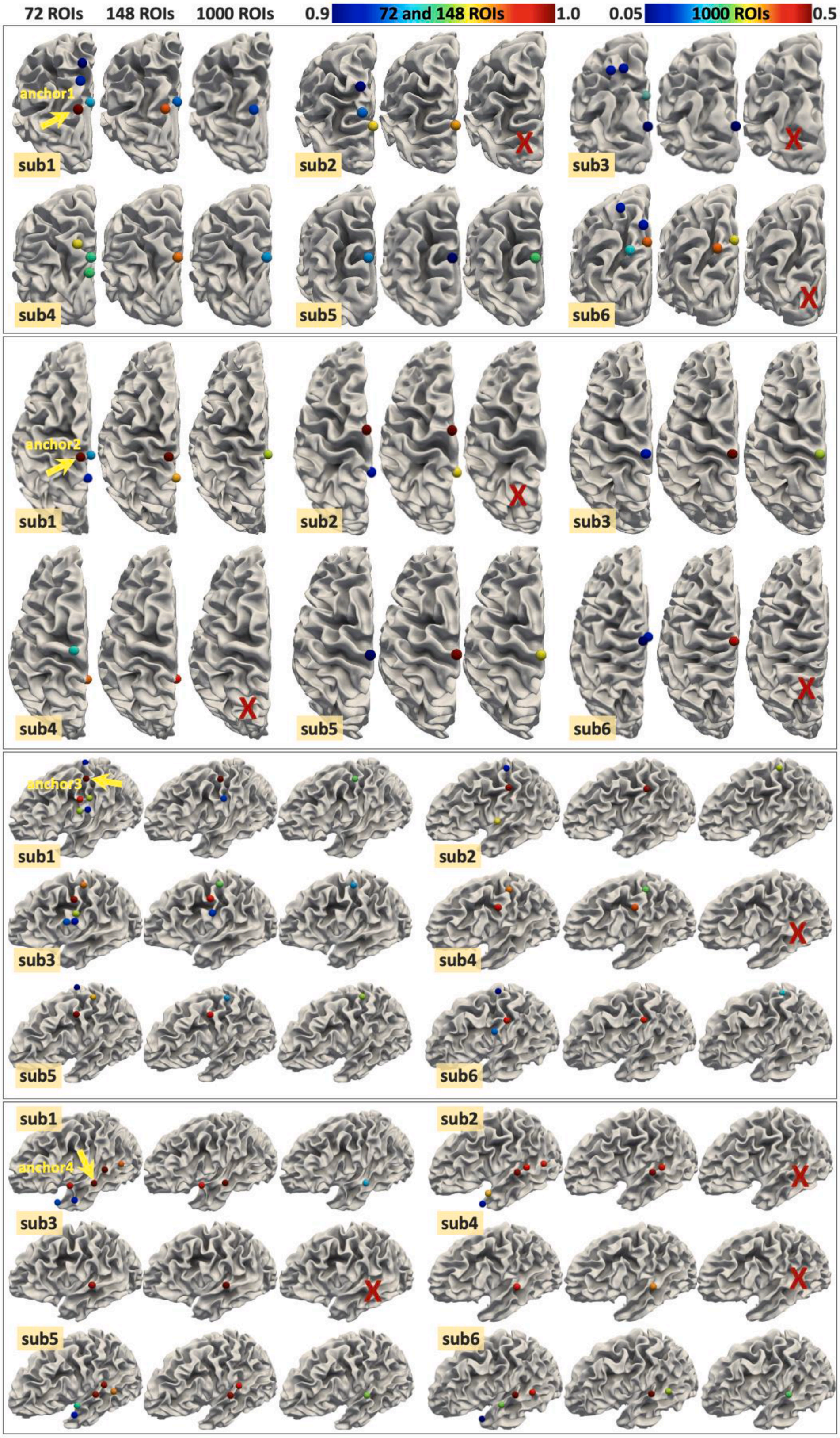

Fig. 10. The results of identified corresponding 3HGs of 4 anchor 3HGs in 6 randomly selected subjects using different brain atlases.

(highlighted by red crosses).

5. Discussion

5.1. Comparison with other transfer learning strategies in medical image analysis

In the evaluation of this study, we try to compare the proposed method with other transfer learning approaches in the field of medical imaging analysis. We observed that existing research predominantly focuses on classification and segmentation tasks (Kora et al. (2022); Atasever et al. (2023)) using diverse medical imaging modalities such as CT (Khan et al. (2021); Liao et al. (2020)), MRI (Deepak et al. (2020); Mehrotra et al. (2020); Plata et al. (2017); Liao et al. (2020)), Ultrasound (Yap et al. (2017); Meng et al. (2020)), and X-rays (Polat et al. (2021)). To handle the image features, the most commonly utilized deep learning models in these studies are CNN-based architectures such as LeNet (Yap et al. (2017)), U-Net (Hervella et al. (2020); Liao et al. (2020)), AlexNet (Deepak et al. (2020); Mehrotra et al. (2020); Plata et al. (2017)), VGGNet (Deepak et al. (2020); Meng et al. (2020)), ResNet (Deepak et al. (2020); Mehrotra et al. (2020); Liao et al. (2020)), GoogLeNet (Deepak et al. (2020); Mehrotra et al. (2020)), DenseNet (Khan et al. (2021); Polat et al. (2021)), and SqueezeNet (Mehrotra et al. (2020)). However, our work differs from these studies in terms of the specific problems addressed, the data formats used, and the models applied. Transfer learning is typically implemented through two main methods: weight initialization and fine-tuning. In weight initialization, pretrained model weights trained on different datasets are directly applied and then updated with the new training data. Fine-tuning involves updating only certain layers of the model while keeping others frozen. Successful transfer learning hinges on the similarity of features between the source and target tasks, such as shared image-related characteristics, which allows pretrained models to effectively enhance training efficiency for the target task. As a result, it is hard for us to feed our data, which employs 3HG networks as input to address lifespan brain anatomical correspondence, into these models trained on using medical image features for classification and segmentation tasks to conducted fair comparison. Recent reviews have also noted similar difficulties, revealing that only 13% of transfer learning studies conduct comparisons with other models (Kora et al. (2022)). This underscores the inherent complexities in benchmarking and effectively comparing diverse transfer learning approaches. Consequently, in our results section, we are unable to provide direct comparisons with other works.

5.2. Scalability and applicability of CDC transfer

The proposed CDC transfer framework is designed to provide an effective embedding of 3HGs that can generalize across different datasets. To validate this, we used the Alzheimer's Disease Neuroimaging Initiative (ADNI) dataset, a large, independent dataset that aims to detect and track Alzheimer's disease. We applied the trained model to the ADNI dataset, generating 3HG embedding vectors for 480 newly collected individuals and evaluating the performance in the 3HG lifespan correspondence task. We also used sub0 from the 34W group as the anchor subject and inferred the correspondence in the ADNI subjects. Using the same criteria as in Section 4.3, we identified the corresponding 3HGs for anchor 3HGs and randomly selected eight individuals to display the results in Fig. 11. As in Figs. 5 and 6, the locations of the

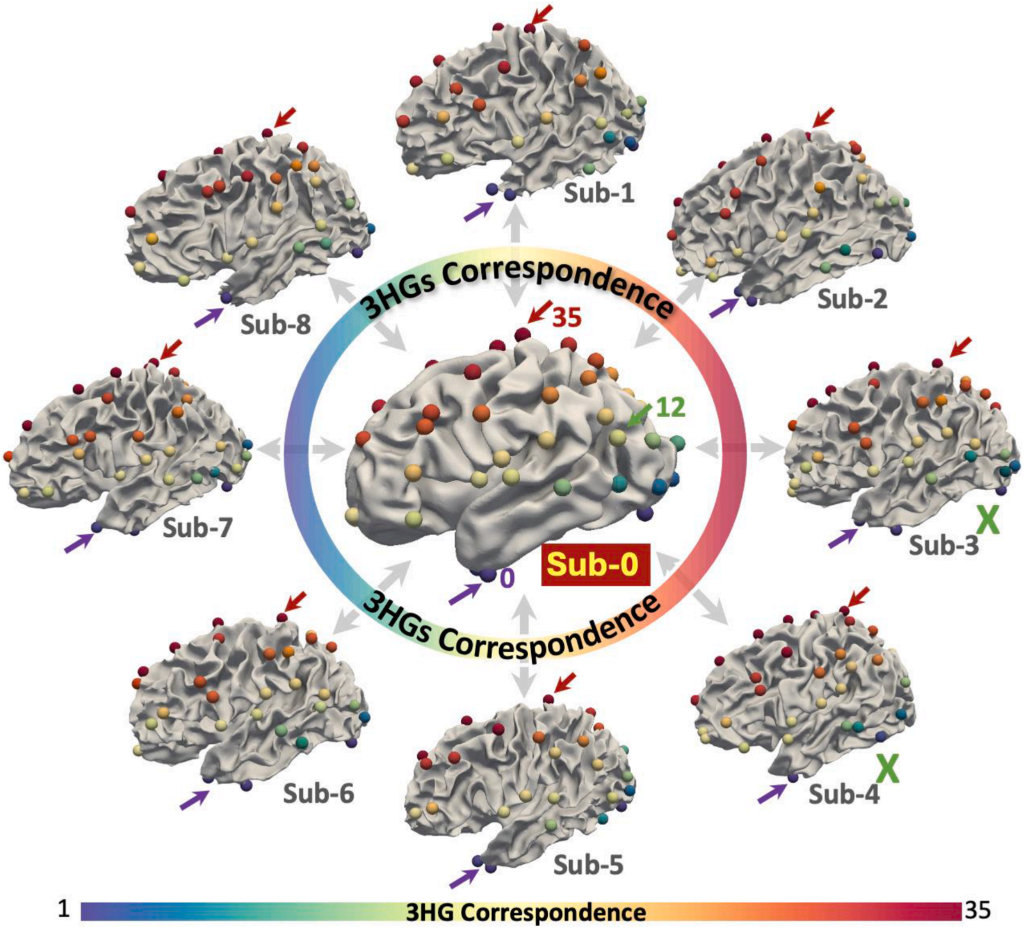

Fig. 11. 3HG lifespan correspondence results of a new independent ADNI dataset.

3HGs are represented by bubbles, and the corresponding 3HGs in different subjects are denoted by the same color. From the results, we can see that the corresponding 3HGs identified in different individuals have consistent locations in terms of common anatomical landmarks. For example, 3HG #0 (marked by purple arrows) and 3HG #35 (marked by red arrows) are found in the front end of the inferior temporal gyri and the top of the postcentral gyri, respectively, across all subjects. However, we also observed that due to individual differences, some anchor 3HGs do not have corresponding 3HGs in other subjects. For example, 3HG #12 does not have corresponding 3HGs in sub-3 and sub-4.

It is worth noting that the ADNI dataset includes different groups, such as elderly normal controls, mild cognitive impairment (MCI) patients, and AD patients. In this experiment, we did not distinguish between the elderly normal controls and patients in the ADNI dataset. Whether the distribution patterns of 3HGs differ between patient groups and normal individuals is a question that remains to be explored and warrants further investigation in future work. In general, the results in Fig. 11 further demonstrate that our proposed CDC transfer framework has good generalizability.

6. Conclusions

In this study, we introduced the cortical developmental continuity (CDC) transfer framework, aiming to leverage the continuous nature of cortical folding development and achieve optimal performance enhancement. Our approach involves transferring ROI feature embeddings across different age groups, following the developmental trajectory of the cerebral cortex. This allows the accumulation and propagation of common patterns while capturing group-specific patterns. To guide the transfer process effectively, we introduced two novel regularizers that facilitate the capture of both common and group-specific patterns.

To evaluate the proposed CDC transfer framework, we conducted experiments using multiple datasets that encompassed four age groups, consisting of over 1,000 brains ranging from 34 gestational weeks to young adult. The experimental results demonstrate the significant improvement in model performance when dealing with populations with limited training samples. Moreover, the CDC transfer learning approach enables robust inference of complex many-to-many anatomical correspondences among different brains at the same or different neurodevelopmental stages. Additionally, the CDC transfer framework offers valuable insights into addressing complex problems that span multiple stages, characterized by a shared underlying inherent relationship alongside considerable cross-stage heterogeneity.

CRediT authorship contribution statement

Lu Zhang: Writing – original draft, Visualization, Validation, Methodology, Investigation, Formal analysis, Data curation, Conceptualization. **Zhengwang Wu:** Writing – review & editing, Data curation. **Xiaowei Yu:** Writing – review & editing. **Yanjun Lyu:** Writing – review & editing. **Zihao Wu:** Writing – review & editing. **Haixing Dai:** Writing – review & editing. **Lin Zhao:** Writing – review & editing. **Li Wang:** Writing – review & editing, Data curation. **Gang Li:** Writing – review & editing, Data curation. **Xianqiao Wang:** Writing – review & editing. **Tianming Liu:** Writing – review & editing, Project administration, Conceptualization. **Dajiang Zhu:** Writing – review & editing, Project administration, Funding acquisition, Conceptualization.

Declaration of competing interest

The authors declare that they have no known competing financial interests or personal relationships that could have appeared to influence the work reported in this paper.

Data availability

I have included the link in the manuscript where the code and data will be released.

Acknowledgements

This work is partially supported by National Institutes of Health (R01AG075582, RF1NS128534, R01MH116225, R01MH117943, RF1MH123202) and National Science Foundation (IIS-2011369).

References

Abdar, M., Samami, M., Mahmoodabad, S.D., Doan, T., Mazoure, B., Hashemifesharaki, R., Liu, L., Khosravi, A., Acharya, U.R., Makarenkov, V., Nahavandi, S., 2021. Uncertainty quantification in skin cancer classification using three-way decision-based Bayesian deep learning. Comput. Biol. Med. 135, 104418.

Atasever, S., Azginoglu, N., Terzi, D.S., Terzi, R., 2023. A comprehensive survey of deep learning research on medical image analysis with focus on transfer learning. Clin. Imaging 94, 18–41.

Blitzer, J., McDonald, R., Pereira, F., 2006. Domain adaptation with struc- tural correspondence learning. In: Proceedings of the 2006 conference on empirical methods in natural language processing, pp. 120–128.

Chen, H., Li, Y., Ge, F., Li, G., Shen, D., Liu, T., 2017. Gyral net: a new representation of cortical folding organization. Med. Image Anal. 42, 14–25.

Deepak, S., Ameer, P.M., 2020. Retrieval of brain MRI with tumor using contrastive loss based similarity on GoogLeNet encodings. Comput. Biol. Med. 125, 103993.

Derrfuss, J., Mar, R.A., 2009. Lost in localization: the need for a universal coordinate database. Neuroimage 48, 1–7.

Desai, R., Liebenthal, E., Possing, E.T., Waldron, E., Binder, J.R., 2005. Volumetric vs. surface-based alignment for localization of auditory cortex ac- tivation. Neuroimage 26, 1019–1029.

Desikan, R.S., Ségonne, F., Fischl, B., Quinn, B.T., Dickerson, B.C., Blacker, D., Buckner, R.L., Dale, A.M., Maguire, R.P., Hyman, B.T., Albert, M.S., 2006. An automated labeling system for subdividing the human cerebral cortex on MRI scans into gyral based regions of interest. Neuroimage 31 (3), 968–980.

Destrieux, C., Fischl, B., Dale, A., Halgren, E., 2010. Automatic parcellation of human cortical gyri and sulci using standard anatomical nomenclature. Neuroimage 53, 1–15.

Díaz-Pernas, F.J., Martínez-Zarzuela, M., Antón-Rodríguez, M., González-Ortega, D., 2021. A deep learning approach for brain tumor classification and segmentation using a multiscale convolutional neural network. In: Healthcare, 9. MDPI, p. 153.

Di Donato, N., Chiari, S., Mirzaa, G.M., Aldinger, K., Parrini, E., Olds, C., Barkovich, A.J., Guerrini, R., Dobyns, W.B., 2017. Lissencephaly: expanded imaging and clinical classification. Am. J. Med. Genetics Part A 173, 1473–1488.

Fischl, B., 2012. Freesurfer. Neuroimage 62, 774–781.

Ge, F., Li, X., Razavi, M.J., Chen, H., Zhang, T., Zhang, S., Guo, L., Hu, X., Wang, X., Liu, T., 2018. Denser growing fiber connections induce 3-hinge gyral folding. Cerebral Cortex 28, 1064–1075.

Giedd, J.N., Rapoport, J.L., 2010. Structural MRI of pediatric brain development: what have we learned and where are we going? Neuron 67, 728–734.

Hervella, Á.S., Rouco, J., Novo, J., Ortega, M., 2020. Learning the retinal anatomy from scarce annotated data using self-supervised multimodal reconstruction. Appl. Soft. Comput. 91, 106210.

Honey, C.J., Thivierge, J.-P., Sporns, O., 2010. Can structure predict function in the human brain? Neuroimage 52, 766–776.

Khan, N.M., Abraham, N., Hon, M., 2019. Transfer learning with intelligent training data selection for prediction of alzheimer's disease. IEEe Access. 7, 72726–72735.

Khan, Z., Yahya, N., Alsaih, K., Ali, S.S.A., Meriaudeau, F., 2020. Evaluation of deep neural networks for semantic segmentation of prostate in T2W MRI. Sensors 20 (11), 3183.

Khan, M.A., Hussain, N., Majid, A., Alhaisoni, M., Chan Bukhari, S.A., Kadry, S., Nam, Y., Zhang, Y.D., 2021. Classification of positive COVID-19 CT scans using deep learning. Comput. Mater. Contin. 66 (3).

Kora, P., Ooi, C.P., Faust, O., Raghavendra, U., Gudigar, A., Chan, W.Y., Meenakshi, K., Swaraja, K., Plawiak, P., Acharya, U.R., 2022. Transfer learning techniques for medical image analysis: a review. Biocybern. Biomed. Eng. 42 (1), 79–107.

LeCun, Y., Bengio, Y., Hinton, G., 2015. Deep learning. Nature 521 (7553), 436–444.

Li, X., Chen, H., Zhang, T., Yu, X., Jiang, X., Li, K., Li, L., Razavi, M.J., Wang, X., Hu, X., et al., 2017. Commonly preserved and species-specific gyral folding patterns across primate brains. Brain Struct. Function 222, 2127–2141.

Liao, X., Qian, Y., Chen, Y., Xiong, X., Wang, Q., Heng, P.A., 2020. MMTLNet: Multi-Modality Transfer Learning Network with adversarial training for 3D whole heart segmentation. Computeriz. Med. Imag. Graphics 85, 101785.

Liu, L., Mou, L., Zhu, X.X., Mandal, M., 2020. Automatic skin lesion classification based on mid-level feature learning. Computeriz. Med. Imag. Graphics 84, 101765.

Long, M., Cao, Y., Wang, J., Jordan, M., 2015. Learning transferable features with deep adaptation networks. In: International conference on machine learning. PMLR, pp. 97–105.

Mehrotra, R., Ansari, M.A., Agrawal, R., Anand, R.S., 2020. A transfer learning approach for AI-based classification of brain tumors. Mach. Learn. Appl. 2, 100003.

Meng, Q., Matthew, J., Zimmer, V.A., Gomez, A., Lloyd, D.F., Rueckert, D., Kainz, B., 2020. Mutual information-based disentangled neural networks for classifying unseen categories in different domains: application to fetal ultrasound imaging. IEEe Trans. Med. ImAging 40 (2), 722–734.

Pan, S.J., Yang, Q., 2009. A survey on transfer learning. IEEe Trans. Knowl. Data Eng. 22, 1345–1359.

Pantazis, D., Joshi, A., Jiang, J., Shattuck, D.W., Bernstein, L.E., Damasio, H., Leahy, R. M., 2010. Comparison of landmark-based and automatic methods for cortical surface registration. Neuroimage 49, 2479–2493.

Peng, J., 2019. Residual convolutional neural network for predicting response of transarterial chemoembolizationin hepatocellular carcinomafrom CT imaging. Cancer Res. 79 (13_Supplement), 1395. -1395.

Plata, D.R., Ramos-Pollan, R., Gonzalez, F.A., 2017. Effective training of convolutional neural networks with small, specialized datasets. J. Intell. Fuzzy Syst. 32 (2), 1333–1342.

Polat, Ç., Karaman, O., Karaman, C., Korkmaz, G., Balcı, M.C., Kelek, S.E., 2021. COVID-19 diagnosis from chest X-ray images using transfer learning: enhanced performance by debiasing dataloader. J. Xray. Sci. Technol. 29 (1), 19–36.

Schaefer, A., Kong, R., Gordon, E.M., Laumann, T.O., Zuo, X.N., Holmes, A.J., Eickhoff, S. B., Yeo, B.T., 2018. Local-global parcellation of the human cerebral cortex from intrinsic functional connectivity MRI. Cerebral Cortex 28 (9), 3095–3114.

Shipp, S., 2007. Structure and function of the cerebral cortex. Curr. Biol. 17, R443–R449.

Stutterd, C.A., Leventer, R.J., 2014. Polymicrogyria: a common and heterogeneous malformation of cortical development. In Am. J. Med. Genetics Part C 166, 227–239. Wiley Online Library.

Van Essen, D.C., 2005. A population-average, landmark-and surface-based (pals) atlas of human cerebral cortex. Neuroimage 28, 635–662.

Van Opbroek, A., Ikram, M.A., Vernooij, M.W., De Bruijne, M., 2014. Transfer learning improves supervised image segmentation across imaging protocols. IEEe Trans. Med. ImAging 34, 1018–1030.

Wang, J., Zhu, H., Wang, S.H., Zhang, Y.D., 2021. A review of deep learning on medical image analysis. Mobile Netw. Appl. 26 (1), 351–380.

Wang, L., Wu, Z., Chen, L., Sun, Y., Lin, W., Li, G., 2023. ibeat v2. 0: a multisite-applicable, deep learning-based pipeline for infant cerebral cortical surface reconstruction. Nat. Protoc. 18, 1488–1509.

Woodworth, R.S., Thorndike, E.L., 1901. The influence of improvement in one mental function upon the efficiency of other functions.(i). Psychol. Rev. 8, 247.

Yap, M.H., Pons, G., Marti, J., Ganau, S., Sentis, M., Zwiggelaar, R., Davison, A.K., Marti, R., 2017. Automated breast ultrasound lesions detection using convolutional neural networks. IEEe J. Biomed. Health Inform. 22 (4), 1218–1226.

Zhang, L., Wang, L., Gao, J., Risacher, S.L., Yan, J., Li, G., Liu, T., Zhu, D., Initiative, A.D. N., et al., 2021. Deep fusion of brain structure-function in mild cognitive impairment. Med. Image Anal. 72, 102082.

Zhang, L., Wang, L., Zhu, D., 2020a. Jointly analyzing alzheimer's disease related structure-function using deep cross-model attention network. In: 2020 IEEE 17th International Symposium on Biomedical Imaging (ISBI). IEEE, pp. 563–567.

Zhang, L., Wang, L., Zhu, D., 2020b. Recovering brain structural connectivity from functional connectivity via multi-GCN based generative adversarial network. In: Medical Image Computing and Computer Assisted Intervention– MICCAI 2020: 23rd International Conference, 2020. Springer, Lima, Peru, pp. 53–61. October 4–8Proceedings, Part VII 23.

Zhang, L., Wang, L., Zhu, D., Initiative, A.D.N., et al., 2022. Predicting brain structural network using functional connectivity. Med. Image Anal. 79, 102463.

Zhang, L., Zhao, L., Liu, D., Wu, Z., Wang, X., Liu, T., Zhu, D., 2023. Cortex2vector: anatomical embedding of cortical folding patterns. Cerebral Cortex 33, 5851–5862.

Zhang, T., Huang, Y., Zhao, L., He, Z., Jiang, X., Guo, L., Hu, X., Liu, T., 2020c. Identifying cross-individual correspondences of 3-hinge gyri. Med. Image Anal. 63, 101700.

Zhang, T., Li, X., Jiang, X., Ge, F., Zhang, S., Zhao, L., Liu, H., Huang, Y., Wang, X., Yang, J., et al., 2020d. Cortical 3-hinges could serve as hubs in cortico-cortical connective network. Brain ImAging Behav. 14, 2512–2529.

Zhou, S.K., Greenspan, H., Shen, D., 2023. Deep learning for medical image analysis. Academic Press.